

Construction and modeling of a reconfigurable MRI coil for lowering SAR in patients with deep brain stimulation implants

Laleh Golestanirad^{a,b,*}, Maria Ida Iacono^c, Boris Keil^{a,d}, Leonardo M. Angelone^c,
Giorgio Bonmassar^{a,b}, Michael D. Fox^e, Todd Herrington^g, Elfar Adalsteinsson^{a,f},
Cristen LaPierre^a, Azma Mareyam^a, Lawrence L. Wald^{a,b}

^a Athinoula A. Martinos Center for Biomedical Imaging, Department of Radiology, Massachusetts General Hospital, Boston, MA, USA

^b Harvard Medical School, Boston, MA, USA

^c Division of Biomedical Physics, Office of Science and Engineering Laboratories, Center for Devices and Radiological Health, US Food and Drug Administration, Silver Spring, MD, USA

^d Institute of Medical Physics and Radiation Protection, THM, Life Science Engineering, Giessen, Germany

^e Berenson-Allen Center for Noninvasive Brain Stimulation, Beth Israel Deaconess Medical Center and Harvard Medical School, Boston, MA, USA

^f Electrical Engineering and Computer Science, Massachusetts Institute of Technology, 77 Massachusetts Avenue, Cambridge, MA, USA

^g Partners Neurology, Massachusetts General Hospital, Brigham and Women's Hospital, Harvard Medical School, Boston, MA, USA

ARTICLE INFO

Keywords:

Deep brain stimulation (DBS)
Finite element method (FEM)
Magnetic resonance imaging (MRI)
Medical implants
Neurostimulation
Parkinson's disease
RF heating
Safety
Specific absorption rate (SAR)

ABSTRACT

Post-operative MRI of patients with deep brain stimulation (DBS) implants is useful to assess complications and diagnose comorbidities, however more than one third of medical centers do not perform MRIs on this patient population due to stringent safety restrictions and liability risks. A new system of reconfigurable magnetic resonance imaging head coil composed of a rotatable linearly-polarized birdcage transmitter and a close-fitting 32-channel receive array is presented for low-SAR imaging of patients with DBS implants. The novel system works by generating a region with low electric field magnitude and steering it to coincide with the DBS lead trajectory. We demonstrate that the new coil system substantially reduces the SAR amplification around DBS electrodes compared to commercially available circularly polarized coils in a cohort of 9 patient-derived realistic DBS lead trajectories. We also show that the optimal coil configuration can be reliably identified from the image artifact on B_1^+ field maps. Our preliminary results suggest that such a system may provide a viable solution for high-resolution imaging of DBS patients in the future. More data is needed to quantify safety limits and recommend imaging protocols before the novel coil system can be used on patients with DBS implants.

Introduction

Deep brain stimulation (DBS) is the therapeutic use of chronic electrical stimulation of the brain via implanted electrodes, most commonly used to treat the motor symptoms of Parkinson's disease (PD), essential tremor, and dystonia (Limousin et al., 1995; Krack et al., 2003; Benabid et al., 1996; Obeso et al., 2001; Herrington et al., 2016). Because of its superb soft-tissue contrast, magnetic resonance imaging (MRI) is excellently poised to assess complications and comorbidities in this patient population. However, the access to post-operative MRI is severely limited for patients with DBS due to safety concerns. Serious complications have been reported (Henderson et al., 2005; Spiegel et al., 2003; Nutt et al., 2001) as a result of the so-called *antenna effect*, where the radiofrequency (RF) fields of the MRI transmitter coupled with long DBS leads and produced excessive tissue

heating (Rezaei et al., 2004; Shellock et al., 2000). Alterations in the lead's design and material properties have been suggested to reduce the heating. Examples of such modifications include use of material with high thermal conductivity which act as a heat-sink (Elwassif et al., 2012), use of coiled wires with distributed air-gaps to increase lead's impedance and thus, reduce heat-generating induced currents (Gray et al., 2005), and use of resistive tapered stripline technology which distributes the RF energy along the lead's length to prevent formation of hotspots at the tip (Serano et al., 2015). In parallel, modifications in the imaging hardware have been proposed. The idea of manipulating the electric field of the MRI RF transmitter to produce low E-field regions in the head which could be steered to contain the DBS implant has shown promising results in proof-of-concept studies (Eryaman et al., 2011; Eryaman et al., 2014; Eryaman et al., 2012; McElcheran et al., 2015). The first prototype of a rotatable MRI birdcage transmit-

* Corresponding author at: A.A. Martinos Center for Biomedical Imaging, Department of Radiology, Massachusetts General Hospital, Boston, MA, USA.
E-mail address: lgolestanirad@gmail.com (L. Golestanirad).

ter developed based on this concept demonstrated significant reduction of SAR amplification around electrode contacts of generic DBS lead models (Golestanirad et al., 2016b).

To date, the applicability of latter methodologies has been demonstrated in studies of simplified implant models with straight path (Golestanirad et al., 2016). In practice however, implanted DBS leads have complex trajectories consisting of intersecting sections and overlapping loops which can potentially affect the specific absorption rate (SAR) of the radiofrequency energy in the tissue. The next step to translate this novel technology for clinical use is a measure of its performance in realistic patient populations. In this paper, a robust computational approach is applied to obtain, for the first time, a quantitative prediction of SAR-reduction performance of the reconfigurable MRI technology in a cohort of realistic patient-derived DBS models.

In what follows, the restrictions of current MRI technology for DBS imaging are discussed, a novel methodology using reconfigurable MRI RF coils for DBS imaging is introduced; the use of finite element modeling (FEM) to predict the performance of reconfigurable MRI coils is explained; a detailed method of image segmentation and DBS model development for FEM simulations is introduced; results of SAR-reduction performance of the reconfigurable MRI coil system in a real patient population are discussed; and a methodology to predict the optimal coil configuration from the B_1^+ image artifact is examined. The paper concludes with a discussion of safety considerations and a brief description of future work for further advancement of the technology.

MRI technologies for DBS imaging: current limitations and novel approaches

The major restriction of present MRI technology for DBS imaging is due to the coupling of the MRI RF transmitters electric field with DBS leads, leading to a high power deposition in the tissue surrounding the electrode contacts, potentially causing excessive heating and tissue damage (Rezai et al., 2004; Shrivastava et al., 2012). To address this concern, post-operative application of MRI on DBS patients is restricted to 1.5 T, and is further constrained in terms of power used during the exam (Medtronic, 2015). These restrictions impose practical challenges, as MRI protocols that optimally image DBS leads and subcortical structures tend to have much higher power than current recommendations allow (Larson et al., 2008). Efforts to reduce the interaction between MRI fields and conductive implants are recent and limited to proof-of-concept studies. In 2011 Eryaman et al. demonstrated the possibility of modifying the electric field of an RF coil to generate regions of low E-field magnitude in the body without significantly altering the transmit sensitivity (Eryaman et al., 2011). In 2012 it was shown that the low tangential electric field region of a linearly-polarized birdcage transmitter can be steered to coincide with a wire implant to reduce the SAR (Eryaman et al., 2012). Recently, we demonstrated that at 1.5 T, this low-field region is thick enough to encompass a generic DBS lead with wire segments that were up to 60° out of plane, reducing the SAR at the implant tip by up to 500 fold below that of commercially available coils (Golestanirad et al., 2016). Based on these preliminary results, we developed the first prototype of a DBS-friendly reconfigurable MRI coil system with a mechanically rotating birdcage transmitter, enabling patient-specific field manipulation, integrated with a 32-channel anthropomorphic receive array for maximum signal reception (Golestanirad et al., 2016). The SAR-reduction in such a coil system is achieved by systematically rotating the transmitter around patient's head to find an optimal rotation angle at which the implant is fully contained in the low E-field region. The performance of this technique however is dependent on the lead trajectory, because even if a portion of the implant remains outside the low E-field region the risk remains that the RF fields couple to the lead. To date, the feasibility of this approach has only been demonstrated for simplified DBS geometries with straight paths. Realistic

DBS leads on the other hand, have complicated trajectories with out-of-plane segments and overlapping loops (Machado et al., 2006). In fact, the presence of loops has been demonstrated to significantly affect the SAR at the electrode tip (Rezai et al., 2004; Shrivastava et al., 2012; Baker et al., 2005; Golestanirad et al., 2016a). An essential question to address for further advancement of this methodology is how well it performs with realistic DBS implant trajectories. In this paper, we present for the first time, numerical simulations of the SAR-reduction performance of a novel reconfigurable MRI technology in a cohort of 9 realistic patient-derived DBS lead models with irregular and complex trajectories.

B_1^+ image artifact as an indicator of SAR

Although MRI scanners report an estimated value of the whole-body SAR for each specific pulse sequence, local SAR hotspots that are correlated with tissue heating are not reported. It is important to note, however, that the same currents induced on the DBS lead that are the cause of heating also produce image artifacts. van den Bosch and Griffin have shown that for elongated metallic implants positioned parallel to the static magnetic field, the magnitude or phase of the image artifact in B_1^+ field maps can be used to predict quantitative values of the RF currents induced on the implant, which in turn, correlate with tissue heating (van den Bosch et al., 2010; Griffin et al., 2015; Nordbeck et al., 2009). The visual artifact in B_1^+ field maps have been also shown to correlate with the local SAR for planar (Eryaman et al., 2014) and simplified DBS lead models (Golestanirad et al., 2016). However, because the image artifact's shape and location is dependent on the implant trajectory and its orientation with respect to the magnetic field, it is important to verify that the B_1^+ field maps can be reliably used to predict the optimal rotation angle in realistic patient populations. In this paper we introduce a methodology that uses averaged samples of B_1^+ field magnitude around the implant to predict the transmit coil optimal rotation angle for SAR reduction. We show that this technique reliably predicts the coil position for SAR minimization independent of the location of B_1^+ sampling.

Materials and methods

Reconfigurable MRI coil: construction and characteristics

The reconfigurable head coil is composed of a mechanically rotating linearly-polarized birdcage transmitter and a close-fitting 32-channel receive array. The 16-rung low-pass birdcage was constructed on a 35 cm-diameter acrylic cylinder. The birdcage frame was 3D-printed (Fortus 360, Stratasys, Eden Prairie, MN) and incorporated a rotation mechanism to align the low E-field region of the coil with the implant trajectory. Two mechanical annuli (blue, in Fig. 1), one with axial holes equally spaced 5° apart, were secured to the birdcage ends and rested on four-guide wheels located on a sliding frame, allowing the birdcage to rotate freely around its axis without touching the receive array. Once the desired rotation has been obtained, a locking pin is inserted into the rotation lock mechanism through an axial hole, securing the birdcage in the desired position. The entire assembly rests on two guide rails, allowing the birdcage to be moved to facilitate subject access to the array coil.

A 12-mm copper tape was used to construct the typical ladder network of the birdcage. The coil had a length of 30 cm and each leg used two 10 pF capacitors in series (Series 25, Voltronics, Danville, NJ, USA), one at each end of the rung, which tuned the primary mode to 64 MHz. A variable capacitor was placed opposite to the drive port in order to allow the coil to be fine-tuned. 50 Ω impedance-matching was achieved using a series capacitor while the coil was loaded with an anthropomorphic head phantom. The latter was filled with a mixture of 4.5% \pm 5% liter distilled H₂O, 40.50 g NaCl (purity 98%, Sigma-Aldrich Corp., St. Louis, MO) and 1.2 kg of edible agar powder (Golden Coin

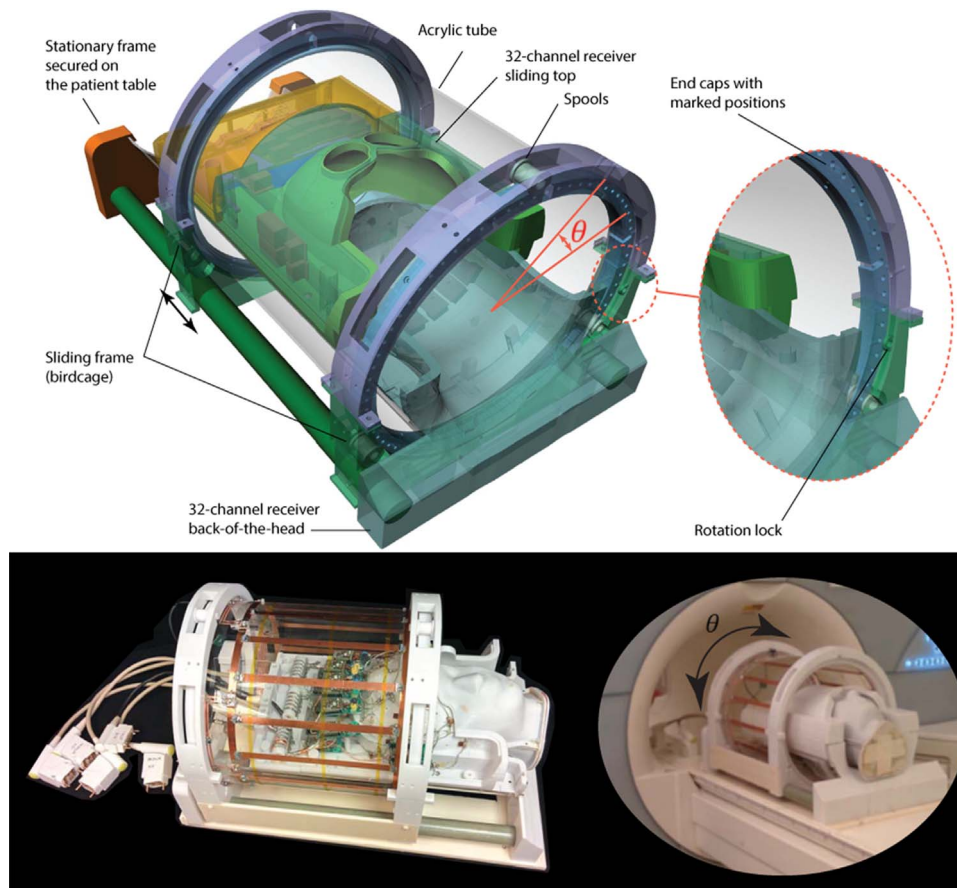


Fig. 1. Top row: CAD model of reconfigurable MRI coil housing. The birdcage slides back and forth on a stationary frame to facilitate patient's access to the receive coil. Two mechanical annuli secured at the ends of the acrylic tube rest on installed in the frame, allowing the birdcage to rotate freely around its axis without touching the receive array. Bottom row: Views of the assembled coil on the bench and inside the scanner. (For interpretation of the references to color in this figure legend, the reader is referred to the web version of this article.)

Agar Agar Powder, Capital Food International, Inc., Santa Fe Springs, CA). The electrical properties of the phantom were measured using a network analyzer (ENA series, Agilent Technologies, Santa Clara, CA) with a high temperature dielectric probe (85070E kit, Agilent Technologies, Santa Clara, CA) and were representative of the averaged human head ($\epsilon_r = 66.34$ and $\sigma = 0.49$ S/m). A PIN diode detuning circuit was incorporated in order to switch off the transmit coil while receiving with the receive array.

The 32-channel receiver array coil was built similarly to our previous works (Keil et al., 2013; Keil and Wald, 2013). In brief, a closefitting array was obtained using a design based on a 3D surface reconstruction of averaged segmented anatomical MRIs from 20 representative subjects followed by the creation of the model in acrylonitrile butadiene styrene plastic using a 3D printer. The layout of the overlapped circular coil elements was guided by a hexagonal and pentagonal tiling pattern (Wiggins et al., 2006). Each loop element was divided symmetrically into three parts, and reconnected with high-Q tuning chip capacitors (Series 11, Voltronics, Salisbury, MD, USA) (Fig. 2). The matching network consisted of a capacitive voltage divider, matching the element's output under loaded conditions to noise-matched impedance of the preamplifier (i.e., 50Ω). A self-shielded resonant figure-eight coaxial cable-trap was placed between the coil element and the preamplifier to suppress common modes on the cable. Active detuning was achieved using a PIN diode in series with a hand-wound inductor L , which together with a matching capacitor C_m resonated at the Larmor frequency. Finally, a low-pass lumped-element phase-shifter was designed and inserted into the circuit to transform the low impedance of a low-noise preamplifier (Siemens AG, Healthcare, Erlangen, Germany) to a high impedance at the coil terminal to reduce induced currents from flowing on the loop

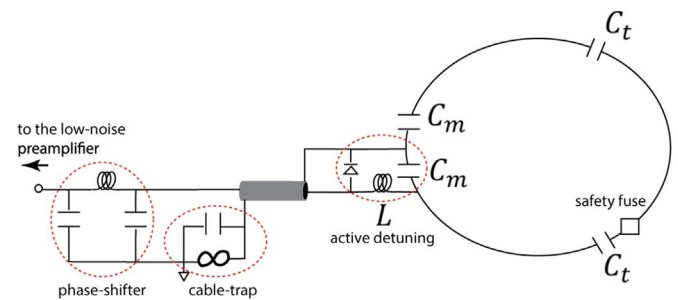


Fig. 2. A circuit schematic of a receive element with cable trap to suppress the common mode, active detuning, and preamplifier decoupling networks. A fuse was inserted to the circuit for additional protection of the subject.

due to coupling with other loop elements (Roemer et al., 1990). The latter provided a powerful decoupling mechanism for next-nearest neighbor coil elements. In addition to the active detuning provided by the PIN diode, a 570 mA fuse was integrated serially into each loop element to ensure safety. Five standard coil plugs (Odu, Mueldorf, Germany) were used to connect the ensemble to the MRI scanner (Siemens Avanto). Each plug's cable incorporated an additional common mode cable trap to avoid interaction with the birdcage transmitter.

Numerical models: MRI coil and patient-derived DBS leads

Finite element method (FEM) simulations were performed to investigate the SAR-reduction performance of the reconfigurable coil

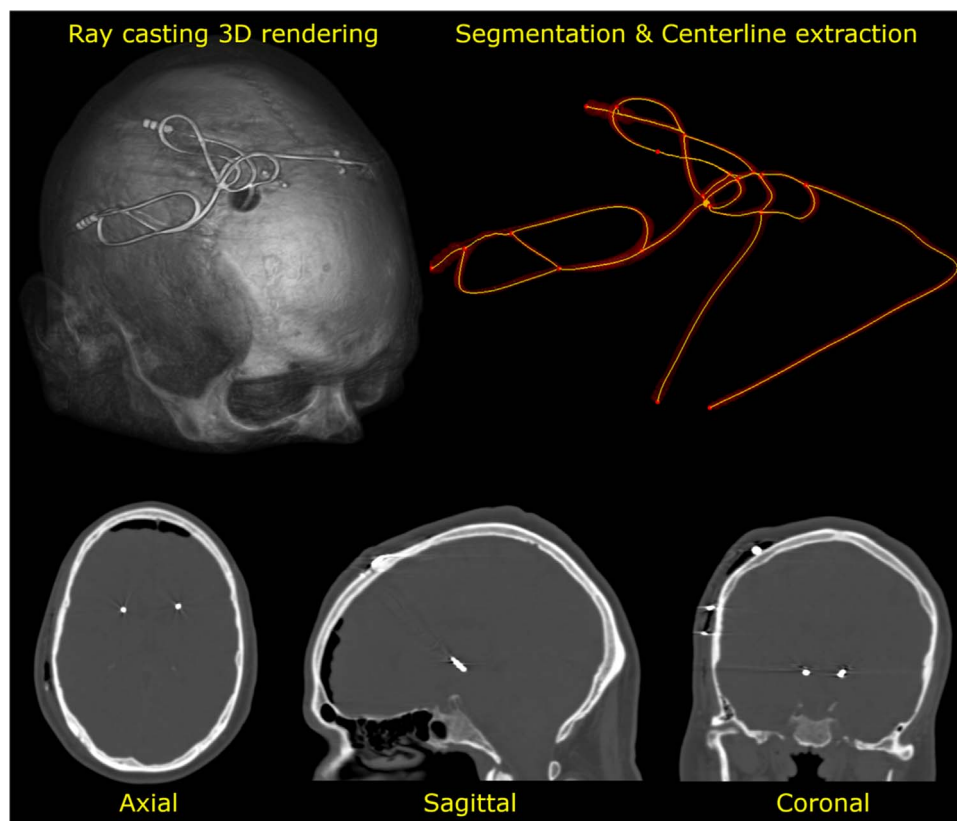


Fig. 3. Steps of DBS lead segmentation. Top row: 3D view of post-operative CT images of a patient with the implant and segmented path after image contrast threshold and manual refinement to recover overlapping loop segments. Bottom row: 2D views of post-operative CT images showing DBS lead artifact.

system in a cohort of 9 patient-derived DBS models. Only the transmit coil was modelled for SAR calculations, since inclusion of the 32-channel receive array has been shown to have a negligible effect on the SAR (Golestanirad et al., 2016b). ANSYS Electronic Desktop (HFSS 16.2, Designer, ANSYS Inc., Canonsburg, PA) was used to implement an integrated numerical approach combining FEM simulation with RF circuit-analysis to tune and match the coil at 64 MHz. A detailed description of this technique can be found in (Golestanirad et al., 2016b; Kozlov and Turner, 2009). Secondary use of patient data for modeling and simulation of DBS leads was approved by Massachusetts General Hospital (MGH) Internal Review Board. Nine realistic DBS lead trajectories and head models were semi-automatically segmented from intra-operative CT images of patients operated on for sub-thalamic nucleus DBS at Massachusetts General Hospital. Amira 3D (Amira 5.4, FEI Inc.) was used for initial image segmentation and 3D surface construction of the head. A thresholding algorithm based on an intensity histogram analysis was applied to extract the silhouette of the head and a preliminary mask of the hyperdense DBS lead from the CT images (Fig. 3). The results of the segmentation were refined using semi-automatic tools, including holes/gap filling, island removing, and opening and closing morphological operations. A manifold triangulated surface model of the head was generated using the Amira's built-in marching cubes algorithm. The model was smoothed and simplified and was assigned the electric properties of the average human head ($\epsilon_r=66.34$ and $\sigma=0.49$ S/m).

The masks of the leads contained several topological defects due to the presence of self-intersecting sections and overlapping loops and required further processing. First, the centerline of the lead was estimated using a skeletonization algorithm followed by a smooth curve-fitting algorithm (Simpleware Ltd., UK). Then the intersecting segments of the centerline were manually adjusted to assure a minimum distance between segments greater than the lead diameter (1.27mm). Once the lead trajectories were extracted for each patient,

they were imported into ANSYS HFSS and models of electrode contact, core, and insulation were constructed around them. Models were composed of four cylindrical contacts (outer diameter=1.27 mm, wall thickness=150 μm), connected through a solid straight central core (diameter=260 μm) (Fig. 4b). Electrode contacts were made of 90%:10% platinum-iridium (Pt:Ir $\sigma = 4 \times 10^6$ S/m), separated by a polyurethane insulation ($\sigma = 10^{-10}$ S/m, $\epsilon_r=3.5$ (Elwassif et al., 2006)) and were positioned 0.5 mm apart (Medtronic, 2003).

A total of 90 simulations were performed: 9 patient-derived DBS lead trajectories at 10 coil configurations. Fig. 7 shows the DBS lead trajectories and head models. The coil's rotation angle θ was uniformly increased with $\Delta\theta = 10^\circ$ from $\theta = 0^\circ$ (feed cable in front of patient's nose) to $\theta = 90^\circ$ (feed cable in front of patient's ear) (Fig. 4a). For comparison, simulations were also performed for a conventional circularly polarized (CP) birdcage with and without the DBS lead. Only one orientation of the CP birdcage coil was modelled with feed cables located at $\theta = 0^\circ$ and $\theta = 90^\circ$ positions. A 90° phase lag between input signals produced a counter-clockwise rotating B_1 field. (when looking from top of the head toward the head).

For each simulation, the FEM solver was set up to generate an initial tetrahedral mesh with a very fine resolution on the DBS lead (maximum tetrahedron edge < 0.5 mm). An adaptive mesh algorithm followed, refining the mesh by 30% between each two iterations. Mesh refinement continued until the maximum difference of the calculated S-parameters between two consecutive simulations was below 0.01. Fig. 4 gives details of the MRI coil dimension and rotation angle, position of patient's head and DBS lead inside the coil, and topology of DBS electrode contacts, their interconnections, and the FEM mesh.

SAR calculations

The total power absorbed in the head was calculated by computing the volume integral of the loss density in the head. The whole-head-

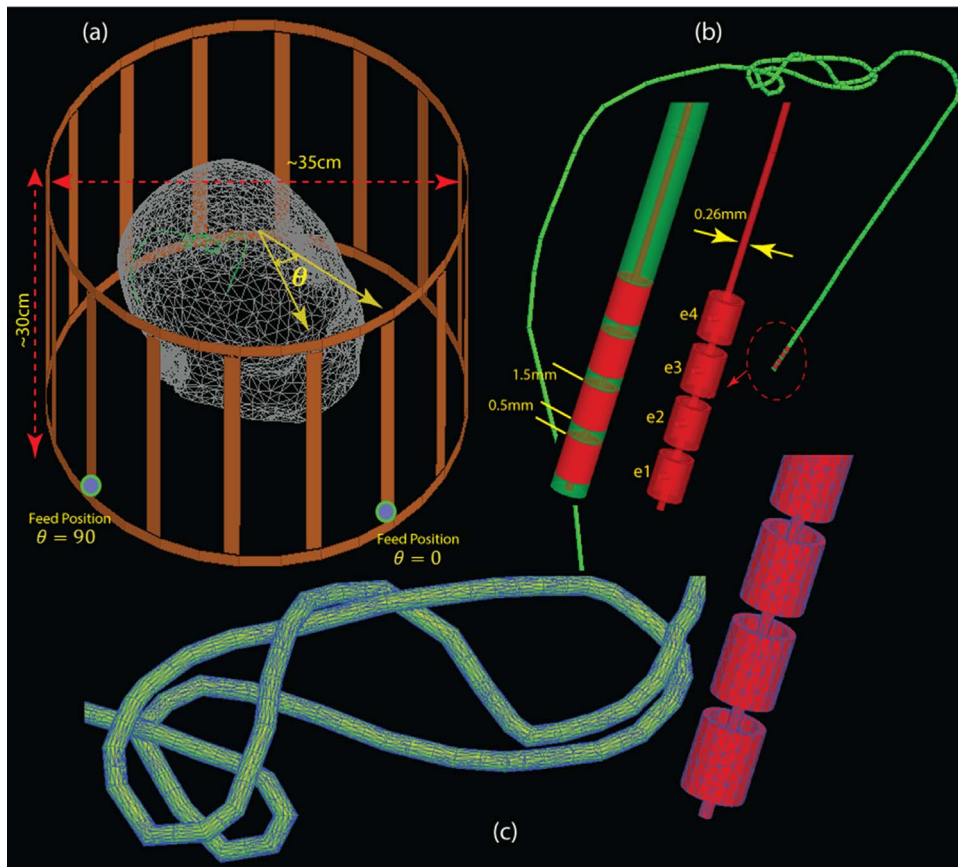


Fig. 4. (a) FEM setup showing the head model and implant inside the transmit coil. The rotation angle of LP birdcage and feed positions of CP birdcage are illustrated. (b) Details of DBS lead model including electrode contacts, core and insulation. (c) Sample of a FEM adaptive mesh after convergence was reached. Mesh was inspected visually for all simulations to assure fine details of DBS lead were properly captured.

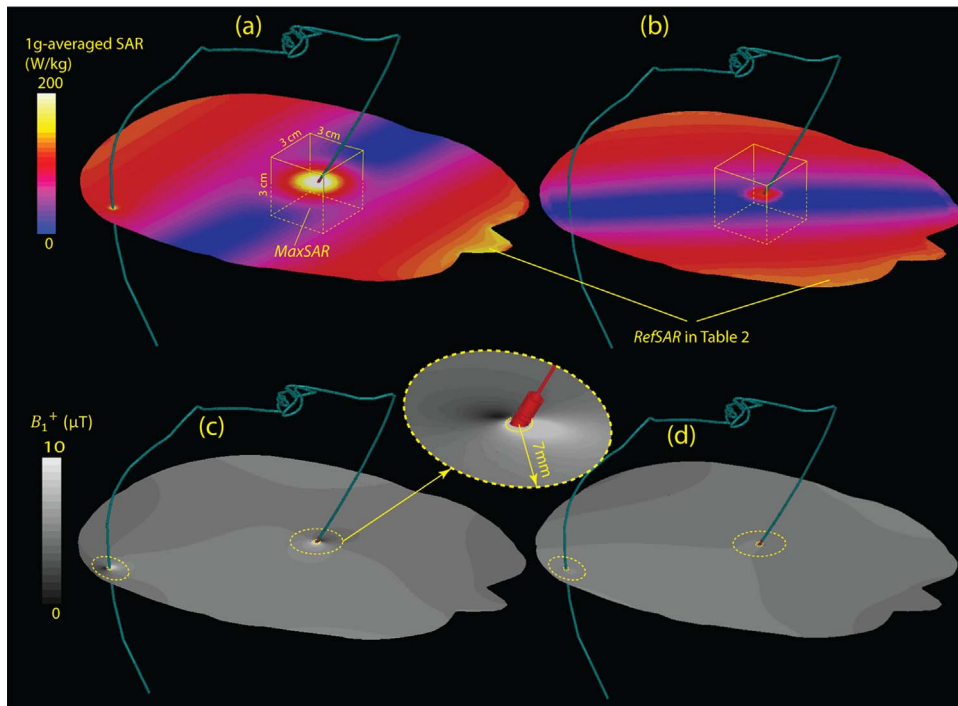


Fig. 5. (a) & (b) Examples of $MaxSAR$ and $RefSAR$ calculated for model ID7 with rotating birdcage at default ($\theta = 0^\circ$) and optimum ($\theta = 40^\circ$) positions. (c) & (d) Example of visual B_1^+ artifact, ΔB_1^+ , calculated around conductive contact e3 and the posterior insulated section of the lead for patient ID7. ΔB_1^+ is shown for with rotating birdcage at default ($\theta = 0^\circ$) and optimum ($\theta = 40^\circ$) position.

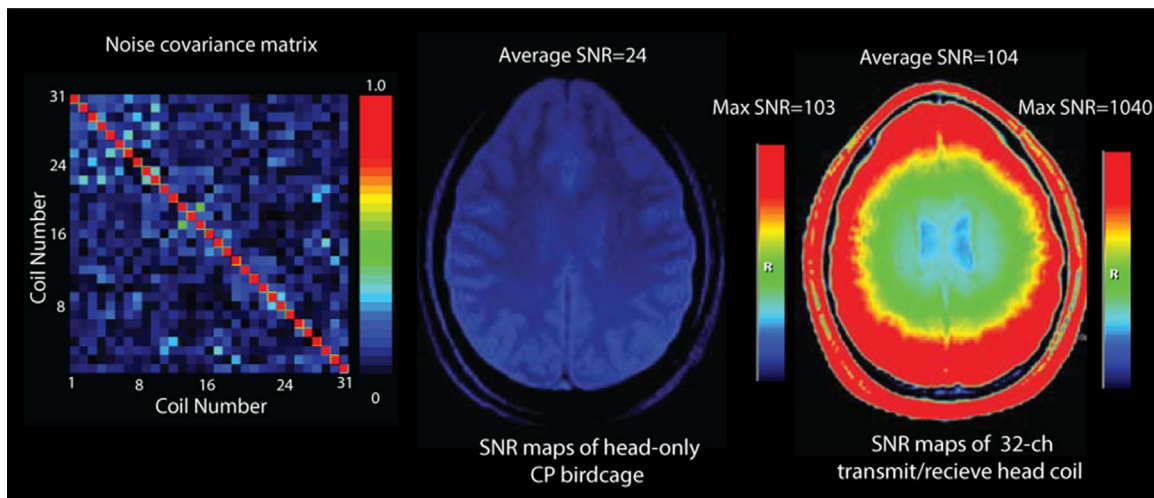


Fig. 6. Noise covariance matrix and SNR maps of the reconfigurable birdcage coil. SNR maps of a head-only CP birdcage is given for comparison.

averaged SAR (SAR_w) was then calculated by dividing this total absorbed power by the head mass:

$$whSAR = \frac{1/2 \iiint_{Head\ Volume} \sigma |E|^2}{head\ mass} \quad (1)$$

where $|E|$ is the magnitude of electric field phasor and σ is the conductivity of the tissue. 1g-averaged SAR was calculated according to IEEE STD P1528.4 recommendation (IEEE, 2014), using the built-in SAR calculation module in ANSYS HFSS 16.2). HFSS calculates the local SAR at each mesh point as:

$$SAR = \frac{1}{2\rho} \sigma \|E\|^2 \quad (2)$$

where E is the magnitude of the electric field phasor, ρ is the density of the material and σ is the material conductivity. The 1g-averaged SAR was calculated over a volume that surrounded each mesh point. The volume was determined by the material's mass density to contain 1 g mass.

For each patient, we first calculated the spatial root mean square (rms) of the magnitude of the B_1^+ field on an axial plane passing through the center of the head model without the implant in a CP birdcage that produced the maximum allowable whole-head SAR of 3.2 W/kg (Zaremba, 2001). The peak magnitude of the B_1^+ field vector was sampled with a 1 mm \times 1 mm resolution from this axial plane and samples were used to calculate the B_1^+ rms as:

$$B_1^+ rms = \sqrt{\frac{\sum_N |B_{1N}^+|^2}{N}} \quad (3)$$

where $|B_{1N}^+|$ is the peak magnitude of the Nth sample and the summation is over all samples. For all other simulations, the input power of the coil was adjusted to generate the same magnitude of B_1^+ rms on this reference plane.

The maximum local SAR (referred to as $MaxSAR$) was then calculated as the maximum of the 1g-averaged SAR in a $30 \times 30 \times 30$ mm³ volume that encompassed all four electrode contacts (Fig. 5a). To have a reference for comparison, we also calculated the maximum 1g-averaged SAR (referred to as $RefsAR$) in the head outside of this cubic region, on an axial plane passing through the distal electrode contact.

Quantification of B_1^+ image artifact

The counter clockwise rotating component of the RF magnetic field was computed as $B_1^+ = 0.5(B_{1x} + jB_{1y})$ Hoult (2000) and recorded from two axial planes: one passing through the center of the distal electrode

contact (electrode “e1” in Fig. 4b) and the other passing through the center of the electrode contact “e3”. The strength of the visual B_1^+ artifact was quantified as a scalar number ΔB_1^+ calculated over two circular regions (radius=7 mm) on each axial plane, one centered at the conductive electrode contact, and one centered at the posterior insulated section of the lead. The B_1^+ amplitudes in each circular region were sampled with 0.5 mm resolution. ΔB_1^+ was then defined as

$$\Delta B_1^+ = k \frac{\bar{B}_{1Max_n}^+ - \bar{B}_{1Min_n}^+}{B_{1Max}^+} \quad (4)$$

where $\bar{B}_{1Max_n}^+$ is the average of n largest values of B_1^+ in the region, $\bar{B}_{1Min_n}^+$ is the average of n smallest values of B_1^+ in the region, B_{1Max}^+ is the maximum value of B_1^+ , and k is a constant used for visualization.

Results

Reconfigurable coil

The transmit coil was tuned and matched only once with the feed cable at $\theta = 0^\circ$ position. Rotation of the coil slightly changed the magnitude of the one-port reflection coefficient S_{11} ; however no further adjustment was made for different rotation angles. The receive coil had a mean noise correlation of 10% between elements. The ensemble of transmit-receive coil went through a safety test protocol developed in our laboratory, routinely applied to assess the quality and safety of lab-made coils at Massachusetts General Hospital. This protocol was used to assess the quality of active detuning and SNR maps, as well as evaluating temperature increases. The temperature rise, both in the coil circuitry due to currents and in the head phantom due to RF absorption remained below 2 °C during long continuous scans (~15 min). Fig. 6 displays the SNR maps of the reconfigurable coil system with the feed at $\theta = 0^\circ$ position. There was no significant difference between SNR maps at different rotation angles. SNR maps of a circularly polarized one-channel head-only birdcage coil is given for comparison.

Numerical models: accuracy, convergence, and mesh statistics

The integrated computational approach adopted in this work has been shown to accurately predict the RF field distribution of MRI birdcage coils (less than 1% error in prediction of loaded and unloaded scattering parameters, less than 15% error in prediction of absolute field values) (Golestanirad et al., 2016b). All simulations converged with fewer than eight adaptive passes. Once converged, the mesh was inspected visually to ensure that all fine details of DBS lead and insulation were properly represented (Fig. 4c). DBS lead lengths varied

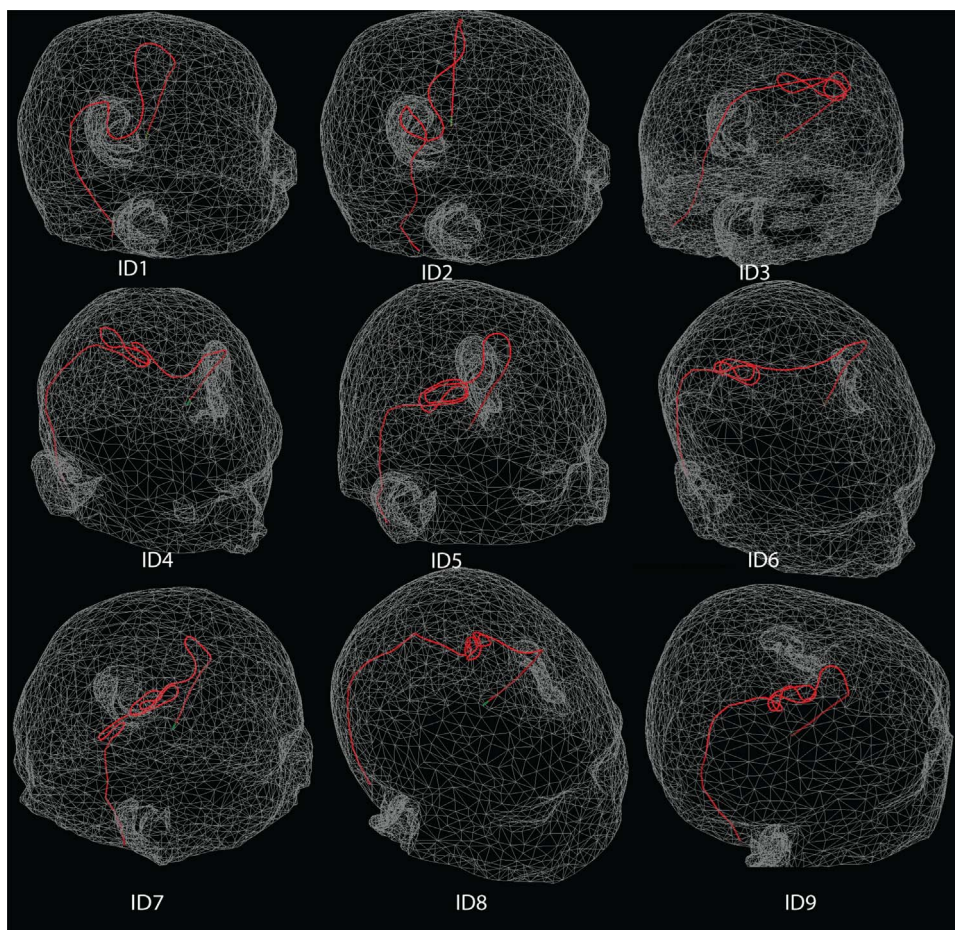


Fig. 7. Patient-derived head models. Lead trajectories and head silhouette were extracted from post-operative CT images.

Table 1

Mesh statistics for the DBS lead, insulation and head model in a representative simulation (ID5, $\theta = 0^\circ$). Mesh statistics were similar across simulations.

	No. Tets	Min edge length [mm]	Max edge length [mm]	RMS edge length [mm]	Min Tet. Vol. [mm ³]	Max Tet. Vol. [mm ³]	Mean Tet. Vol. [mm ³]
DBS Lead (core & contacts)	36678	0.1	0.8	0.4	2.1e-6	4.7e-3	7.5e-4
DBS Insulation	134252	0.1	2.5	0.6	2.06e-6	74.7e-3	4.2e-3
Head	251933	0.2	11.3	6.0	7.3e-5	76.1	13.1

over a range from 38 cm to 55 cm (mean \pm standard deviation 49.2 cm \pm 5.9 cm) and the average head volume was 3.5 l \pm 0.3 l. Table 1 gives the mesh statistics for a representative simulation, including number of tetrahedral elements, minimum, maximum and root mean square of tetrahedral edge lengths, and minimum, maximum and mean of tetrahedral element volumes. Mesh statistics were similar across all simulations.

SAR reduction performance and B_1^+ field artifact

Fig. 8 shows the $MaxSAR$ in the reconfigurable LP birdcage as a function of the rotation angle (solid blue lines) and the $MaxSAR$ in the CP birdcage with and without the implant (dashed purple lines) for each patient-derived simulation. In an LP birdcage that produced the same B_1^+ rms as a CP birdcage operating at its maximum allowable power, the $MaxSAR$ was 4.5 \pm 1.8 W/kg (averaged over all DBS lead trajectories) when the coil was in its optimal rotation angle. The $MaxSAR$ of a CP birdcage operating at its maximum power (i.e., whole-head SAR=3.2 W/kg) with no implant was observed to be 1.1 \pm 0.3 (averaged over all DBS $MaxSAR$ volumes). The reference SAR ($RefSAR$), gave an estimate of the maximum 1g-averaged SAR that

occurred in the head in areas far from the electrode. The $MaxSAR$ in the linear birdcage operating at its optimal rotation angle was always lower than the reference SAR of both the linear birdcage (23.5 \pm 6.6 W/kg, averaged over all DBS lead trajectories) and the CP birdcage without the implant (9.7 \pm 3.5 W/kg, averaged over all DBS lead trajectories). The location of this optimal rotation angle varied for each individual lead trajectory (optimum $\theta = 50 \pm 16^\circ$). Table 2 gives the details of $MaxSAR$, $RefSAR$, whole-head SAR and rms of B_1^+ fields in an exemplary simulation. Fig. 9 gives the mean and standard deviation of $MaxSAR$ and $RefSAR$ of the LP birdcage operating at its optimal rotation angle and the CP birdcage with no implant, averaged over all DBS trajectories.

It is important to note however, that the worst case scenario $MaxSAR$ of the LP birdcage, which occurred when the coil was operated with the feed positioned far from its optimal angle, was significantly higher than the $MaxSAR$ of the CP birdcage. Table 3 gives an example where the worst case scenario $MaxSAR$ of the LP coil is given and compared to the $MaxSAR$ of the CP birdcage. As it can be observed the $MaxSAR$ of the LP birdcage can be up to 85% higher than the CP birdcage if the coil is operated far from its optimal angle.

The visual B_1^+ artifact, quantified as ΔB_1^+ in Eq. 3, was calculated

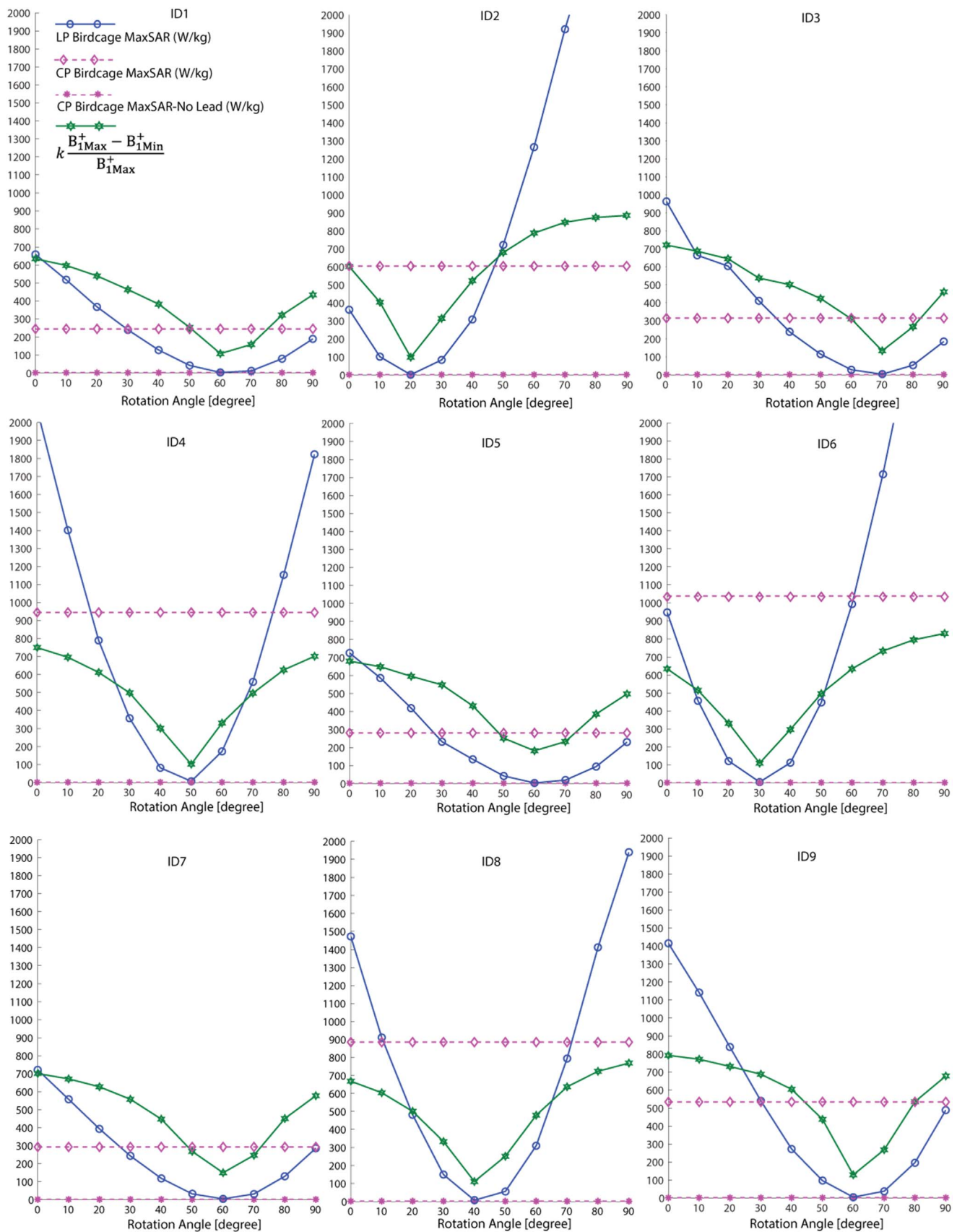


Fig. 8. The evolution of *MaxSAR* (solid blue lines) and the B_{1+} field artifact, ΔB_{1+}^+ (solid green line) as a function of linear birdcage coil rotation angel. *MaxSAR* in head with and without the implant in a circularly polarized birdcage is given for comparison (dashed purple lines). (For interpretation of the references to color in this figure legend, the reader is referred to the web version of this article.)

Table 2

MaxSAR, *RefSAR*, whole-head SAR and rms of B_1^+ field in the reconfigurable LP birdcage, CP birdcage without the DBS implant, and CP birdcage with the DBS implant. Simulation results were similar across subjects.

Patient ID9: DBS lead length=50 cm, head model volume=3.9 l				
LP birdcage rotation angle °	<i>MaxSAR</i> [W/kg]	<i>RefSAR</i> [W/kg]	Whole-head SAR [W/kg]	B_1^+ rms [μ T]
0	1414.8	31.6	6.5	7.1
10	1140.6	30.4	6.3	7.1
20	838.2	29.1	6.2	7.1
30	540.4	27.4	5.7	7.1
40	272.2	26.3	5.6	7.1
50	97.1	24.4	5.5	7.1
60	4.9	21.6	5.5	7.1
70	38.2	19.2	5.5	7.1
80	196.8	20.2	5.8	7.1
90	488.6	22.2	6.0	7.1
CP birdcage with DBS lead	534.3	10.5	3.3	7.1
CP birdcage without DBS lead	0.9	10.4	3.2	7.1

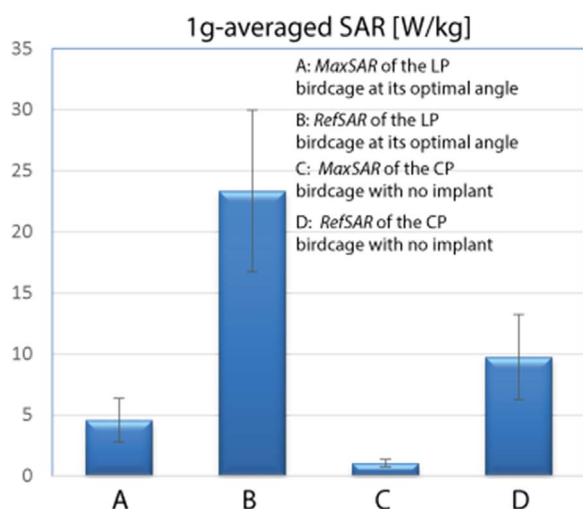


Fig. 9. (A) & (B): *MaxSAR* and *RefSAR* of the linear operating at its optimal rotation angle. The input of the linear birdcage power was adjusted to produce the same rms of B_1^+ fields as a CP birdcage operating at its maximum allowable power for healthy subjects, i.e., whole-head SAR of 3.2 W/kg. (C) & (D): *MaxSAR* and *RefSAR* of a CP birdcage operating at its maximum allowable power in a head with no implant. Data is averaged over all DBS lead trajectories. Error bars represent standard deviation.

Table 3

The worst case *MaxSAR* of the LP birdcage operated at feed angles in the range of 0°–90°, compared with the *MaxSAR* of the CP birdcage. Input power was adjusted for both coils to produce a mean B_1^+ = 7.1 μ T.

Patient ID	Worst case <i>MaxSAR</i> [W/kg] LP birdcage	<i>MaxSAR</i> [W/kg] CP birdcage	% Change
1	658.2	245.6	62
2	4091.0	605.2	85
3	962.4	315.3	67
4	2075.1	945.4	54
5	725.4	281.3	61
6	3311.5	1034.1	68
7	721.7	293.4	59
8	1940.2	884.8	54
9	1414.8	534.4	62

for n=5 averages at four different location: (a) on an axial plane passing through the center of the distal electrode contact “e1” in a circular area centered at the contact, (b) on an axial plane passing through the center

of the distal electrode contact “e1” in a circular area centered at the posterior insulated section of the lead, (c) on an axial plane passing through the center of the electrode contact “e3” in a circular area centered at the electrode contact, and (d) on an axial plane passing through the center of the electrode contact “e3” in a circular area centered around the posterior insulated section of the lead (Fig. 5). For all subjects and at all four locations ΔB_1^+ highly correlated with the *MaxSAR* when the coil’s rotation angle was varied (correlation coefficient $r=0.88 \pm 0.04$). Fig. 8 (green line) gives ΔB_1^+ at location (a) with k set to 1000 for visualization.

Interestingly, we observed that the location of *MaxSAR* was not at the tip of the lead but mostly around electrode contacts “e2” and “e3”. This is in contrast with previous studies which used simple straight wires to model DBS leads and concluded that maximum power deposition always occurs at the tip of the wire (Yeung et al., 2001; Smith et al., 2000; Park et al., 2007; Nitz et al., 2001). Fig. 9 shows the distribution of *MaxSAR* for a representative lead geometry at two different rotation angles (ID9: $\theta = 0^\circ$, $\theta = 90^\circ$). *MaxSAR* distributions were similar across subjects and different rotation angles. We calculated the percent difference in the magnitude of *MaxSAR* and the magnitude of 1g-averaged SAR at a point located at the center of the distal electrode contact and 0.5 mm away from the electrode’s surface (Fig. 10a) *MaxSAR* was 20%–60% higher than the SAR recorded at the electrode tip (mean \pm std = 33 \pm 12%, calculated over all subjects and for both LP birdcage at $\theta = 0^\circ$ and CP coil). The distance r (Fig. 10a) between the location of the *MaxSAR* and the distal electrode tip was 2.7 mm \pm 0.6 mm.

Discussion and conclusion

Although experts practicing in centers performing high volumes of DBS procedures have agreed that MRI is necessary in patients with DBS systems to evaluate new or existing intracranial pathology (Bronstein et al., 2011), more than one third of medical centers do not perform MRI on these patients with the topmost reason stated as stringent industry guidelines and warnings, followed by concerns for liability, risk, and safety (Tagliati et al., 2009). Recently, some manufactures have relaxed their guidelines to allow the use of body coils which was previously prohibited. However, major practical challenges are virtually unaffected as stringent power monitoring remains in place (new guidelines limit the maximum rms of B_1^+ field to 2 μ T and in cases where the scanner does not report the B field, the more conservative whole-head SAR limit of 0.1 W/kg should be applied). Considerable effort has been dedicated to understand and control safety risks by characterising MRI-induced DBS heating accounting for factors such as lead configuration (Rezai et al., 2004; Baker et al., 2005; Shrivastava et al., 2010), lead position with respect to the MRI RF coil (Nitz et al., 2001; Mattei et al., 2008) and variability of reported absorbed power across different MRI systems (Baker et al., 2006). There is however a consensus that the problem has a very large parameter space with many interacting factors which preclude a systematic approach to identify main culprit(s).

Recently, modifications in MRI hardware have been introduced to address this issue. Here we present design, construction and characterization of the ensemble of a reconfigurable transmit-receive head coil with an easy-to-access patient design which aims to lower the SAR during MRI of patients with DBS implants. The close-fit design of the receive array is particularly helpful in restricting the head motion, a problem exacerbated in patients with Parkinson’s disease. The signal-to-noise ratio is superior to the commercially available head-only coils and is comparable to the state-of-the-art 32 channel receive arrays. The SAR reduction performance of the coil system evaluated for the first time in a realistic patient population showed a virtual elimination of SAR amplification around the implant. In all simulations, an optimum coil rotation angle was found that reduced the maximum 1g-averaged SAR at the DBS contacts (referred to as *MaxSAR*) to values below the

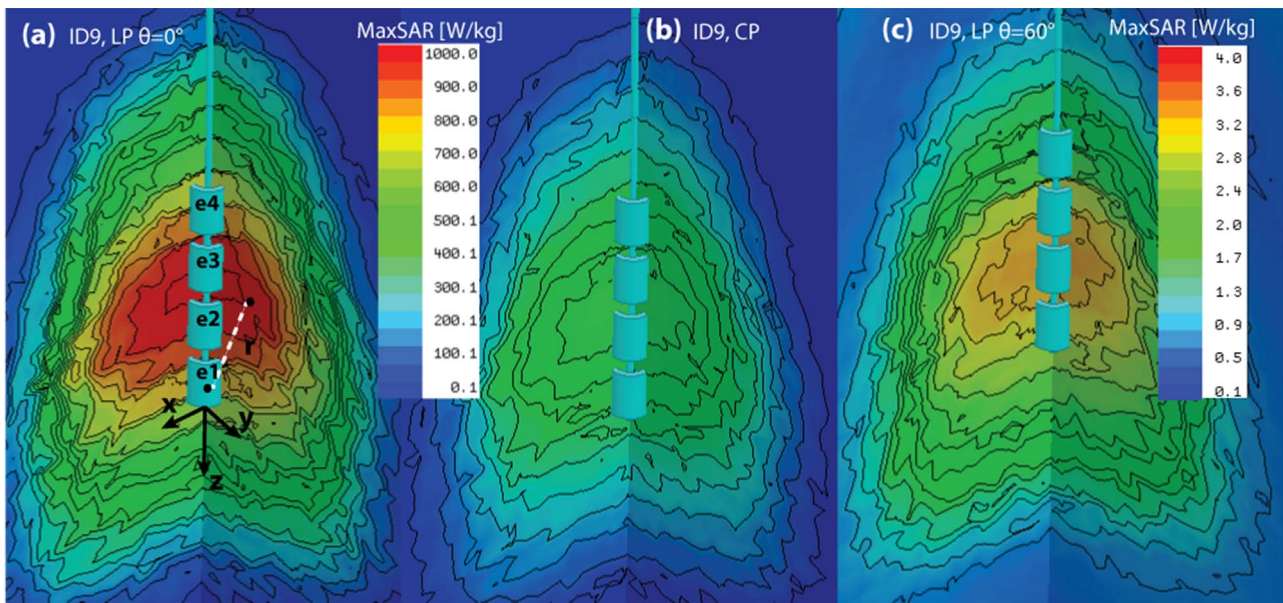


Fig. 10. Distribution of $MaxSAR$ around DBS contacts for a representative patient (ID9) for (a) LP birdcage at $\theta = 0^\circ$ and (b) CP birdcage, and (c) LP birdcage at $\theta = 60^\circ$. $MaxSAR$ distributions were similar across different patients and different rotation angles. The location of maximum SAR was mostly around electrode contacts 2 and 3 with the values 20–60% higher than those recorded at the tip.

maximum 1g-averaged in the head (referred to as $RefSAR$). It is important to mention however, that approaches based on modulation of multiple independent sources such as those proposed in (Eryaman et al., 2012; McElcheran et al., 2015) will allow realization of an elliptical field polarization which could be more effective for leads with substantially out-of-plane segments. Nevertheless, the simplicity of operation of the rotating coil will make it more suitable for clinical applications.

The optimum rotation angle was different for individual subjects, but its whereabouts could be guessed from the trajectory of the implant. A conceivable approach (although computationally intensive) for clinical application of such a coil system is to perform a pre-scan patient-specific simulation using inter- or post-operative CT images, similar to what has been done here, to have a good initial guess of the optimum coil position with respect to patient's head. When patient is in the scanner, a series of low-SAR B_1^+ field mapping pulse sequences could be applied to fine-tune the optimum coil angle based on the B_1^+ field visual artifact. Once the coil is in its optimum configuration, pulse sequences with higher whole-head SAR (SAR_w) deposition or longer duration could be potentially applied. The authors would like to emphasize however, that our current state of knowledge to date does not warrant post-operative use of such coil system on patients with SAR_w values higher than those recommended by the manufacturer. Further investigation is needed to establish safe SAR_w values and application protocols before the novel technology can be used on patients. It is important to note for example, that the $MaxSAR$ values of the LP birdcage when operated at rotation angles far from the optimum position can be substantially higher than those of the CP birdcage (see Table 3). An investigation of the worst case $MaxSAR$ values over all possible rotation angles is required to devise safeguards that minimize the risks associated with maloperation of the coil. By the same token, sensitivity of the SAR-reduction performance to deviations from the optimal rotation angle should be quantified in a larger cohort of realistic lead trajectories. Finally, an uncertainty analysis is required to investigate the degree of SAR reduction when the lead cannot be optimally contained in the low-E field region. The latter is particularly important to determine the maximum electric field that is safe for imaging.

An interesting observation was that maximum SAR_{1g} occurred mostly around electrode contacts “e2” and “e3”, instead of the distal

electrode as expected. Theoretical studies that modelled straight wires (Park et al., 2007; Nitz et al., 2001; Armenean et al., 2004; Yeung et al., 2002) and simulations of simplified DBS lead geometries (Eryaman et al., 2014; Cabot et al., 2013; Mohsin et al., 2008; Angelone et al., 2010) have concluded that maximum SAR occurs at the electrode tip. Consequently, experimental studies assessing heating of DBS leads have mostly measured the temperature rise only at the location of the distal electrode contact (Smith et al., 2000; Mattei et al., 2008; Baker et al., 2004; Finelli et al., 2002). Our simulation results shows that the magnitude of the maximum SAR_{1g} , occurred mostly around second and third contact electrodes could be up to 60% higher than the value measured at the distal tip. Such observation highlights the importance of simulation-derived experiments for safety assessment of medical implants as recently recognized by US Food and Drug Administration. Whenever such approaches are adopted, special attention must be paid to ensure that all structures are meshed with adequate resolution and numerical simulations converged beyond a reasonable threshold.

It is worth noting however that DBS lead models used in the present study do not perfectly mimic actual commercial leads. Medtronic lead model 3389 for example, has spiral cores similar to those presented in (Elwassif et al., 2012). The effect of core topology on the distribution and values of deposited SAR remains to be investigated. While the present study is focused on the effects of lead trajectories, numerical values of SAR resulting from modern leads would likely result in lower numerical values for SAR than those reported here. Another point to note is that lead trajectories simulated here were extracted from inter-operative images before the pulse generator was connected. Once the wires are connected to the pulse generator, their configuration and geometry could slightly change, becoming straighter and more similar to those studied in our previous work (Golestanirad et al., 2016b). Finally, it is important to note that the present study did not evaluate the actual temperature rise in the tissue but rather used the simulated SAR as an indirect indicator of potential heating as routinely done when conductive implants are present. Local SAR values however, do not necessarily directly translate to temperature rise, as factors such as thermal conduction and perfusion should be taken into account (Baker et al., 2004). Consequently, when it comes to patient safety, temperature calculations should be considered alongside with SAR monitoring.

Finally, it is worth commenting on the possibility of extending the proposed methodology to 3 T imaging. Although the inherently less

homogenous distribution of RF fields at 127 MHz could affect the efficiency of SAR reduction in DBS leads that have profiles with substantially out of plane segments, we predict that the outlined methodology lower the SAR at 3 T for the majority of DBS leads. The rotating coil methodology can be also employed to complement lead management strategies that attempt to reduce the heating by optimizing the extracranial profile of the lead (Golestanirad et al., 2016a). More simulation and phantom experiments are needed to evaluate the feasibility of this approach.

Disclaimer

The mention of commercial products, their sources, or their use in connection with material reported herein is not to be construed as either an actual or implied endorsement of such products by the Department of Health and Human Services.

Acknowledgement

This work has been supported by NIH grant K99EB021320, R01EB006847, and P41EB015896.

References

- Angelone, L.M., Ahveninen, J., Belliveau, J.W., Bonmassar, G., 2010. Analysis of the role of lead resistivity in specific absorption rate for deep brain stimulator leads at 3T MRI. *Med. Imaging, IEEE Trans.* 29, 1029–1038.
- Armenean, C., Perrin, E., Armenean, M., Beuf, O., Pilleul, F., Saint-Jalmes, H., 2004. RF-induced temperature elevation along metallic wires in clinical magnetic resonance imaging: influence of diameter and length. *Magn. Reson. Med.* 52, 1200–1206.
- Baker, K.B., Tkach, J.A., Phillips, M.D., Rezaei, A.R., 2006. Variability in RF-induced heating of a deep brain stimulation implant across MR systems. *J. Magn. Reson. Imaging* 24, 1236–1242.
- Baker, K.B., Tkach, J.A., Nyenhuis, J.A., Phillips, M., Shellock, F.G., Gonzalez-Martinez, J., et al., 2004. Evaluation of specific absorption rate as a dosimeter of MRI-related implant heating. *J. Magn. Reson. Imaging* 20, 315–320.
- Baker, K.B., Tkach, J., Hall, J.D., Nyenhuis, J.A., Shellock, F.G., Rezaei, A.R., 2005. Reduction of magnetic resonance imaging-related heating in deep brain stimulation leads using a lead management device. *Neurosurgery* 57, 392–397.
- Benabid, A.L., Pollak, P., Gao, D., Hoffmann, D., Limousin, P., Gay, E., et al., 1996. Chronic electrical stimulation of the ventralis intermedialis nucleus of the thalamus as a treatment of movement disorders. *J. Neurosurg.* 84, 203–214.
- van den Bosch, M.R., Moerland, M.A., Lagendijk, J.J., Bartels, L.W., van den Berg, C.A., 2010. New method to monitor RF safety in MRI-guided interventions based on RF induced image artefacts. *Med. Phys.* 37, 814–821.
- Bronstein, J.M., Tagliati, M., Alterman, R.L., Lozano, A.M., Volkmann, J., Stefani, A., et al., 2011. Deep brain stimulation for Parkinson disease: an expert consensus and review of key issues. *Arch. Neurol.* 68, 165.
- Cabot, E., Lloyd, T., Christ, A., Kainz, W., Douglas, M., Stenzel, G., et al., 2013. Evaluation of the RF heating of a generic deep brain stimulator exposed in 1.5 T magnetic resonance scanners. *Bioelectromagnetics* 34, 104–113.
- Elwassif, M.M., Kong, Q., Vazquez, M., Bikson, M., 2006. Bio-heat transfer model of deep brain stimulation-induced temperature changes. *J. neural Eng.* 3, 306.
- Elwassif, M.M., Datta, A., Rahman, A., Bikson, M., 2012. Temperature control at DBS electrodes using a heat sink: experimentally validated FEM model of DBS lead architecture. *J. neural Eng.* 9, 046009.
- Eryaman, Y., Akin, B., Atalar, E., 2011. Reduction of implant RF heating through modification of transmit coil electric field. *Magn. Reson. Med.* 65, 1305–1313.
- Eryaman, Y., Turk, E.A., Oto, C., Algin, O., Atalar, E., 2012. Reduction of the radiofrequency heating of metallic devices using a dual-drive birdcage coil. *Magn. Reson. Med.*
- Eryaman, Y., Guerin, B., Akgun, C., Herraiz, J.L., Martin, A., Torrado-Carvajal, A., et al., 2014. Parallel transmit pulse design for patients with deep brain stimulation implants. *Magn. Reson. Med.* 73, 1896–1903.
- Finelli, D.A., Rezaei, A.R., Ruggieri, P.M., Tkach, J.A., Nyenhuis, J.A., Hrdlicka, G., et al., 2002. MR imaging-related heating of deep brain stimulation electrodes: in vitro study. *Am. J. Neuroradiol.* 23, 1795–1802.
- Golestanirad, L., Angelone, L.M., Iacono, M.L., Katnani, H., Wald, L.L., and Bonmassar, G., 2016a. Local SAR near deep brain stimulation (DBS) electrodes at 64 MHz and 127 MHz: A simulation study of the effect of extracranial loops. *Magn. Reson. Med.* (In press).
- Golestanirad, L., Keil, B., Ida-Iacono, M., Bonmassar, G., Angelone, L.M., LaPierre, C., 2016. A Patient-adjustable MRI coil for implant-friendly imaging of deep brain stimulation: Design, construction, and patient-specific numerical simulations. In: *Proceedings of the 24th Annual Meeting of International Society of Magnetic Resonance in Medicine (ISMRM)*, Singapore.
- Golestanirad, L., Keil, B., Angelone, L.M., Bonmassar, G., Mareyam, A., Wald, L.L., 2016. Feasibility of using linearly polarized rotating birdcage transmitters and closefitting receive arrays in MRI to reduce SAR in the vicinity of deep brain stimulation implants. *Magn. Reson. Med.*, (vol. In Press).
- Gray, R.W., Bibens, W.T., Shellock, F.G., 2005. Simple design changes to wires to substantially reduce MRI-induced heating at 1.5 T: implications for implanted leads. *Magn. Reson. Imaging* 23, 887–891.
- Griffin, G.H., Anderson, K.J., Celik, H., Wright, G.A., 2015. Safely assessing radiofrequency heating potential of conductive devices using image-based current measurements. *Magn. Reson. Med.* 73, 427–441.
- Henderson, J.M., Tkach, J., Phillips, M., Baker, K., Shellock, F.G., Rezaei, A.R., 2005. Permanent neurological deficit related to magnetic resonance imaging in a patient with implanted deep brain stimulation electrodes for Parkinson's disease: case report. *Neurosurgery* 57, E1063.
- Herrington, T.M., Cheng, J.J., Eskandar, E.N., 2016. Mechanisms of deep brain stimulation. *J. Neurophysiol.* 115, 19–38.
- Hoult, D., 2000. The principle of reciprocity in signal strength calculations—a mathematical guide. *Concepts Magn. Reson.* 12, 173–187.
- IEEE P1528.4™/D1.0, 2014. Recommended Practice for Determining the Peak Spatial Average Specific Absorption Rate (SAR) in the Human Body from Wireless Communications Devices, 30 MHz - 6 GHz: Requirements for Using the Finite-Element Method for SAR Calculations, specifically involving Vehicle Mounted Antennas and Personal Wireless Devices. ed.
- Keil, B., Wald, L.L., 2013. Massively parallel MRI detector arrays. *J. Magn. Reson.* 229, 75–89.
- Keil, B., Blau, J.N., Biber, S., Hoecht, P., Tountcheva, V., Setsompop, K., et al., 2013. A 64-channel 3T array coil for accelerated brain MRI. *Magn. Reson. Med.* 70, 248–258.
- Kozlov, M., Turner, R., 2009. Fast MRI coil analysis based on 3-D electromagnetic and RF circuit co-simulation. *J. Magn. Reson.* 200, 147–152.
- Krack, P., Batir, A., Van Blercom, N., Chabardes, S., Fraix, V., Ardouin, C., et al., 2003. Five-year follow-up of bilateral stimulation of the subthalamic nucleus in advanced Parkinson's disease. *New Engl. J. Med.* 349, 1925–1934.
- Larson, P.S., Richardson, R.M., Starr, P.A., Martin, A.J., 2008. Magnetic resonance imaging of implanted deep brain stimulators: experience in a large series. *Stereotact. Funct. Neurosurg.* 86, 92–100.
- Limousin, P., Pollak, P., Benazzouz, A., Hoffmann, D., Le Bas, J., Perret, J., et al., 1995. Effect on parkinsonian signs and symptoms of bilateral subthalamic nucleus stimulation. *Lancet* 345, 91–95.
- Machado, A., Rezaei, A.R., Kopell, B.H., Gross, R.E., Sharan, A.D., Benabid, A.L., 2006. Deep brain stimulation for Parkinson's disease: surgical technique and perioperative management. *Mov. Disord.* 21, S247–S258.
- Mattei, E., Triventi, M., Calcagnini, G., Censi, F., Kainz, W., Mendoza, G., et al., 2008. Complexity of MRI induced heating on metallic leads: experimental measurements of 374 configurations. *Biomed. Eng. online* 7, 11.
- McElcheran, C.E., Yang, B., Anderson, K.J., Golestanirad, L., Graham, S.J., 2015. Investigation of parallel radiofrequency transmission for the reduction of heating in long conductive leads in 3 T magnetic resonance imaging. *PLoS One* 10, e0134379.
- Medtronic, 2003. in *Implant Manual: Lead kit for deep brain stimulation*, ed.
- Medtronic, 2015. *MRI Guidelines for Medtronic DeepBrain Stimulation Systems*. (http://manuals.medtronic.com/wcm/groups/mdtcom_sg/@ematerials/@era/@neuro/documents/documents/contrib_228155.pdf), ed Date of access: 12/09/2015.
- Mohsin, S.A., Sheikh, N.M., Saeed, U., 2008. MRI-induced heating of deep brain stimulation leads. *Phys. Med. Biol.* 53, 5745.
- Nitz, W.R., Oppelt, A., Renz, W., Manke, C., Lenhart, M., Link, J., 2001. On the heating of linear conductive structures as guide wires and catheters in interventional MRI. *J. Magn. Reson. Imaging* 13, 105–114.
- Nordbeck, P., Weiss, L., Ehses, P., Ritter, O., Warmuth, M., Fidler, F., et al., 2009. Measuring RF-induced currents inside implants: impact of device configuration on MRI safety of cardiac pacemaker leads. *Magn. Reson. Med.* 61, 570–578.
- Nutt, J., Anderson, V., Peacock, J., Hammerstad, J., Burchiel, K., 2001. DBS and diathermy interaction induces severe CNS damage. *Neurology* 56, 1384–1386.
- Obeso, J.A., Olanow, C.W., Rodriguez-Orez, M.C., Krack, P., Kumar, R., Lang, A.E., 2001. Deep brain stimulation of the subthalamic nucleus or the pars interna of the globus pallidus in Parkinson's disease. *N. Engl. J. Med.* 345, 956–963.
- Park, S.M., Kamondetdacha, R., Nyenhuis, J.A., 2007. Calculation of MRI-induced heating of an implanted medical lead wire with an electric field transfer function. *J. Magn. Reson. Imaging* 26, 1278–1285.
- Rezaei, A.R., Phillips, M., Baker, K.B., Sharan, A.D., Nyenhuis, J., Tkach, J., et al., 2004. Neurostimulation system used for deep brain stimulation (DBS): mr safety issues and implications of failing to follow safety recommendations. *Investigative Radiol.* 39, 300–303.
- Roemer, P.B., Edelstein, W.A., Hayes, C.E., Souza, S.P., Mueller, O.M., 1990. The NMR phased array. *Magn. Reson. Med.* 16, 192–225.
- Serano, P., Angelone, L.M., Katnani, H., Eskandar, E., Bonmassar, G., 2015. A novel brain stimulation technology provides compatibility with MRI. *Sci. Rep.* 5.
- Shellock, F.G., Hatfield, M., Simon, B.J., Block, S., Wamboldt, J., Starewicz, P.M., et al., 2000. Implantable spinal fusion stimulator: assessment of MR safety and artifacts. *J. Magn. Reson. Imaging* 12, 214–223.
- Shrivastava, D., Abosch, A., Hanson, T., Tian, J., Gupta, A., Iaizzo, P.A., et al., 2010. Effect of the extracranial deep brain stimulation lead on radiofrequency heating at 9.4 T (400.2 MHz). *J. Magn. Reson. Imaging* 32, 600–607.
- Shrivastava, D., Abosch, A., Hughes, J., Goerke, U., DelaBarre, L., Visaria, R., et al., 2012. Heating induced near deep brain stimulation lead electrodes during magnetic resonance imaging with a 3 T transverse volume head coil. *Phys. Med. Biol.* 57, 5651.
- Smith, C.D., Kildishev, A.V., Nyenhuis, J.A., Foster, K.S., Bourland, J.D., 2000. Interactions of magnetic resonance imaging radio frequency magnetic fields with

- elongated medical implants. *J. Appl. Phys.* 87, 6188–6190.
- Spiegel, J., Fuss, G., Backens, M., Reith, W., Magnus, T., Becker, G., et al., 2003. Transient dystonia following magnetic resonance imaging in a patient with deep brain stimulation electrodes for the treatment of Parkinson disease. *J. Neurosurg.* 99, 772–774.
- Tagliati, M., Jankovic, J., Pagan, F., Susatia, F., Isaias, I.U., Okun, M.S., et al., 2009. Safety of MRI in patients with implanted deep brain stimulation devices. *Neuroimage* 47, T53–T57.
- Wiggins, G., Wiggins, C., Potthast, A., Alagappan, V., Kraff, O., Reykowski, A. et al., 2006. A 32 channel receive-only head coil and detunable transmit birdcage coil for 7 Tesla brain imaging. In *Proceedings of the ISMRM*, p. 415.
- Yeung, C.J., Susil, R.C., Atalar, E., 2001. RF safety of wires in interventional MRI: using a safety index. *Magn. Reson. Med.* 47, 187–193.
- Yeung, C.J., Susil, R.C., Atalar, E., 2002. RF heating due to conductive wires during MRI depends on the phase distribution of the transmit field. *Magn. Reson. Med.* 48, 1096–1098.
- Zaremba, L., 2001. FDA guidance for MR system safety and patient exposures: current status and future considerations. In: *Shellock, Frank G., Bradley, William G. (Eds.), Magnetic Resonance Procedures: Health Effects and Safety.* CRC Press, Boca Raton, pp. 183–196.